DAVID A. SÁNCHEZ-HERNÁNDEZ
STEVEN R. BEST • MANOS M. TENTZERIS
SUNGTEK KAHNG • GERT F. PEDERSEN

SMART ANTENNAS FOR 5G+

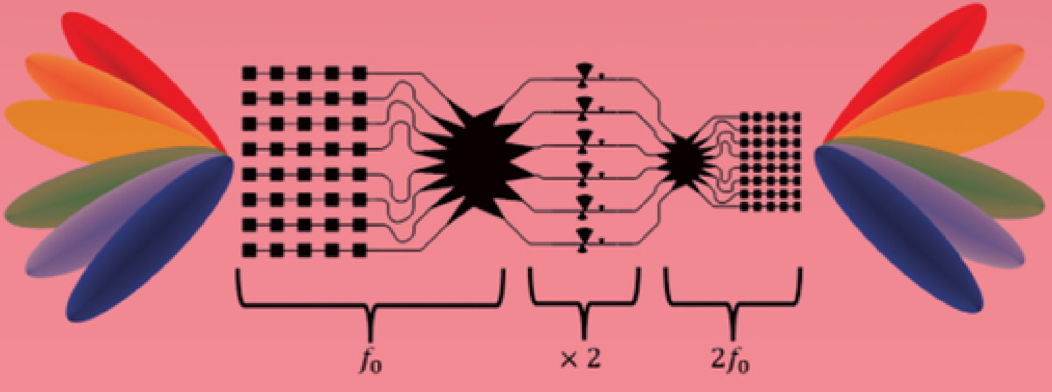

IEEE PRESS

WILEY

Smart Antennas for 5G+

IEEE Press
445 Hoes Lane
Piscataway, NJ 08854

IEEE Press Editorial Board
Sarah Spurgeon, *Editor-in-Chief*

Moeness Amin
Jón Atli Benediktsson
Adam Drobot
James Duncan
Ekram Hossain
Brian Johnson
Hai Li
James Lyke
Joydeep Mitra
Desineni Subbaram Naidu
Tony Q. S. Quek
Behzad Razavi
Thomas Robertazzi
Diomidis Spinellis

Smart Antennas for 5G+

David A. Sánchez-Hernández
Universidad Politécnica de Cartagena
Spain

Steven R. Best
The MITRE Corporation
Bedford, MA
USA

Manos M. Tentzeris
Georgia Institute of Technology
USA

Sungtek Kahng
Incheon National University
South Korea

Gert F. Pedersen
Aalborg University
Denmark

IEEE*Press*
WILEY

Copyright © 2024 by The Institute of Electrical and Electronics Engineers, Inc. All rights reserved.

Published by John Wiley & Sons, Inc., Hoboken, New Jersey.
Published simultaneously in Canada.

No part of this publication may be reproduced, stored in a retrieval system, or transmitted in any form or by any means, electronic, mechanical, photocopying, recording, scanning, or otherwise, except as permitted under Section 107 or 108 of the 1976 United States Copyright Act, without either the prior written permission of the Publisher, or authorization through payment of the appropriate per-copy fee to the Copyright Clearance Center, Inc., 222 Rosewood Drive, Danvers, MA 01923, (978) 750-8400, fax (978) 750-4470, or on the web at www.copyright.com. Requests to the Publisher for permission should be addressed to the Permissions Department, John Wiley & Sons, Inc., 111 River Street, Hoboken, NJ 07030, (201) 748-6011, fax (201) 748-6008, or online at http://www.wiley.com/go/permission.

Trademarks: Wiley and the Wiley logo are trademarks or registered trademarks of John Wiley & Sons, Inc. and/or its affiliates in the United States and other countries and may not be used without written permission. All other trademarks are the property of their respective owners. John Wiley & Sons, Inc. is not associated with any product or vendor mentioned in this book.

Limit of Liability/Disclaimer of Warranty: While the publisher and author have used their best efforts in preparing this book, they make no representations or warranties with respect to the accuracy or completeness of the contents of this book and specifically disclaim any implied warranties of merchantability or fitness for a particular purpose. No warranty may be created or extended by sales representatives or written sales materials. The advice and strategies contained herein may not be suitable for your situation. You should consult with a professional where appropriate. Neither the publisher nor author shall be liable for any loss of profit or any other commercial damages, including but not limited to special, incidental, consequential, or other damages. Further, readers should be aware that websites listed in this work may have changed or disappeared between when this work was written and when it is read. Neither the publisher nor authors shall be liable for any loss of profit or any other commercial damages, including but not limited to special, incidental, consequential, or other damages.

For general information on our other products and services or for technical support, please contact our Customer Care Department within the United States at (800) 762-2974, outside the United States at (317) 572-3993 or fax (317) 572-4002.

Wiley also publishes its books in a variety of electronic formats. Some content that appears in print may not be available in electronic formats. For more information about Wiley products, visit our web site at www.wiley.com.

Library of Congress Cataloging-in-Publication Data

Names: Sánchez-Hernández, David A., author.
Title: Smart antennas for 5G+ / David A. Sánchez-Hernández [and four others].
Description: Hoboken, New Jersey : Wiley, [2024] | Includes index.
Identifiers: LCCN 2024022160 (print) | LCCN 2024022161 (ebook) | ISBN 9781394210503 (hardback) | ISBN 9781394210534 (adobe pdf) | ISBN 9781394210527 (epub)
Subjects: LCSH: Adaptive antennas. | 5G mobile communication systems.
Classification: LCC TK7871.67.A33 S26 2024 (print) | LCC TK7871.67.A33 (ebook) | DDC 621.3841/35–dc23/eng/20240617
LC record available at https://lccn.loc.gov/2024022160
LC ebook record available at https://lccn.loc.gov/2024022161

Cover Design: Wiley
Cover Image: © Diagram of the Rotman-based harmonic mmID. Characterization of gain and angular coverage for the Rotamn lens operating at 14 GHz (reproduced from [Lynch, 2022a] with permission)

Set in 9.5/12.5pt STIXTwoText by Straive, Chennai, India

Contents

List of Figures *ix*
About the Authors *xix*
Foreword *xxiii*
Acknowledgements *xxv*
List of Acronyms *xxix*

1 Introduction: The Path to 5G and Beyond *1*
David A. Sánchez-Hernández and Steven R. Best
Introduction *1*

2 The 5G Physical Layer *13*
Steven R. Best
2.1 Introduction *13*
2.2 The Physical and Data Link Layers *17*
2.3 1G to 4G Cellular Networks *19*
2.4 5G *22*
2.5 Massive MIMO *24*
2.6 The Importance of Antennas in 5G *26*
2.6.1 The 5G gNodeB Advanced Antenna System (AAS) *27*
2.6.2 Antennas for Sub-7 GHz 5G FR1 User Equipment *32*
2.6.3 Antennas for mmWave 5G FR2 User Equipment *33*
2.7 5G mmWave Link Budget Example (Downlink) *35*
2.8 Conclusions *37*

3 Fully Integrated 5G Broadband Antennas and Wireless Modules *39*
Manos M. Tentzeris and Charles A. Lynch
3.1 Introduction *39*

3.2 Broadband Antennas Covering the mmWave Bands for 5G and B5G Applications *41*
3.2.1 3D and Inkjet Printing Broadband 5G AiP *41*
3.2.2 Additive Manufacturing 5G Module with Broadband AiP *46*
3.2.3 Semi-Additive Manufacturing Broadband 5G AiP on Glass Substrate *52*
3.3 Additively Manufactured Shape-Changing Reconfigurable Frequency Selective Surfaces for mmWave/5G Applications *56*
3.3.1 A Fully Inkjet-Printed FSSs Based on Origami “Eggbox” Structure with Four Degrees of Freedom *58*
3.3.2 Novel 4D-Printed Miura-ori Origami-Inspired FSS Structure *63*
3.4 5G+ Integrated Wireless Modules for Communications, Powering, and Sensing Applications *64*
3.4.1 Energy-Autonomous Dual Rotman Lens-Based Harmonic mmID for Ultra-Long-Range Sensing *64*
3.4.2 “Smart” Packaged Localizable mmIDs *69*
3.5 Additively Manufactured Massively Scalable Electronic Steerable Antenna Arrays for Reconfigurable Intelligent Surfaces *72*
3.6 Rotman Lens-Based 5G-Enabled Wireless Power Grid *77*
3.7 Conclusions *81*

4 Metamaterial 5G Beamforming Antennas *83*
Sungtek Kahng
4.1 Mobile Handset Antennas for Sub-6-GHz Bands of B5G and 6G *83*
4.2 Millimeter Wave Antennas for B5G and 6G *103*
4.3 Metamaterial Antennas for B5G and 6G *122*
4.4 Comparative OTA Test Results for B5G and 6G Antennas *128*
4.5 Conclusions *142*

5 Key Performance Indicators for 5G+ Terminal Antennas *145*
David A. Sánchez-Hernández
5.1 Introduction *145*
5.2 5G OTA Test Methods So Far *146*
5.3 The Challenges for Effective 5G+ OTA Testing *156*
5.3.1 Fully Integrated Antenna Arrays *156*
5.3.2 DUT Form Factors *157*
5.3.3 Spatial Agility *159*
5.3.4 Channel Modeling *160*
5.4 Some Effective 5G+ Key Performance Indicators *161*
5.4.1 Averaged Spectral Efficiency *161*
5.4.2 Beamforming SNR Increase (BSNRI) *163*

5.4.3 Beamforming Battery Consumption *163*
5.4.4 Beamforming Temperature Increase *163*
5.4.5 Beamforming Capacity Gain *166*
5.4.6 Beamforming Averaged Latency *169*
5.4.7 End-to-End Latency *170*
5.4.8 RF Latency *172*
5.4.9 DL/UL FTP/TCP/UDP Throughput *173*
5.4.10 True Throughput *174*
5.4.11 Peak Downlink Throughput *174*
5.4.12 Peak Uplink Throughput *175*
5.5 Conclusions *176*

6 Effective Testing of 5G Radios and Antennas *179*
Gert F. Pedersen and Wei Fan
6.1 Introduction *179*
6.2 Calibration Testing of the 5G Antenna Systems *180*
6.2.1 Experimental Comparison of On–Off and All-On Calibration Modes *180*
6.2.1.1 Measurement Campaign *182*
6.2.1.2 Measurement Results *185*
6.2.2 All-on Calibration Methods *186*
6.2.2.1 Complex Signal-based Measurement *186*
6.2.3 Amplitude-only Measurement *193*
6.3 Performance Testing of 5G Radios *195*
6.3.1 Standardization Processing in 3GPP *196*
6.3.1.1 Measurement Methodologies *197*
6.3.1.2 Channel Models *202*
6.3.2 MPAC Results for 5G *207*
6.3.2.1 Channel Validation Results *207*
6.3.2.2 Typical Throughput Testing Results in 5G Trials *210*
6.3.3 CATR Results for 5G *215*
6.3.3.1 Working Principle *215*
6.3.3.2 Validation *224*
6.3.3.3 5G Test Results *227*
6.4 Conclusions *232*

7 Conclusions and Future Challenges *235*
David A. Sánchez-Hernández, Steven R. Best, Manos M. Tentzeris, Sungtek Kahng, and Gert F. Pedersen
7.1 Conclusions and Future Challenges for 5G+ Radio System Testing *235*

7.1.1 Antenna Design and Manufacturing Challenges *236*
7.1.2 Standardized Testing *238*
7.1.2.1 MPAC *238*
7.1.2.2 RTS *239*
7.1.2.3 RC *240*
7.1.2.4 CATR *240*
7.1.3 Non-standardized Testing *241*

References *243*
Index *261*

List of Figures

Figure 2.1 High level block diagram of the transmit side of a communication link. *19*

Figure 2.2 Depiction of the 96-element massive MIMO array and its generic beam pattern. *25*

Figure 2.3 8 × 8, 64-element dual-polarized AAS implementation. *28*

Figure 2.4 MIMO modes of the 8 × 8, 64-element dual-polarized AAS. *29*

Figure 2.5 Depiction of the 8 × 8, 64-element dual-polarized AAS in the usual spherical coordinate system. *30*

Figure 2.6 Generic traffic beam patterns for MIMO modes (a) 2T2R and (b) 4T4R for an 8 × 8 array. *31*

Figure 2.7 Generic traffic beam patterns for MIMO modes (a) 8T8R and (b) 16T16R for an 8 × 8 array. *31*

Figure 2.8 Generic traffic beam patterns for MIMO modes (a) 32T32R and (b) 64T64R for an 8 × 8 array. *31*

Figure 2.9 Generic broadcast beam patterns for MIMO mode 2T2R for an 8 × 8 array. *32*

Figure 2.10 Depiction of the 3GPP 8-panel mmWave MIMO array. *33*

Figure 2.11 Depiction of a 16-element mmWave UE array and its boresight beam pattern. *34*

Figure 2.12 Depiction of a 16-element mmWave UE array and a scanned beam pattern. *35*

Figure 3.1 (a) The effects of exposure time on the 3D-printed flexible substrates (b) Demonstration of massive production, and (c) Flexibility of 3D-printed substrate. *41*

Figure 3.2 The silver nanoparticle ink adhesion (a) without surface treatment and (b) after applying UV ozone surface treatment. *42*

Figure 3.3 The silver conductor printing quality (a) without SU-8 coating and (b) with a thin layer of SU-8 coating. *43*

Figure 3.4 (a) The fabrication process of the proposed additive manufacturing 5G broadband AiP and (b) the proof-of-concept samples. *44*

Figure 3.5 (a) The measured scattering parameters and (b) gain of the proposed broadband 5G antenna. *45*

Figure 3.6 (a) The schematic of the 5G energy harvester SiP with broadband AiP using fully AM multilayered packaging and (b) the fabrication process. *47*

Figure 3.7 (a) 3D-printed substrate with 3D structures including cavity, ramps, and via holes, (b) coating substrate with SU-8, (c) inkjet-printed silver on the top of the 3D-printed substrate, (d) component attachment, (e) cavity filling with flexible 3D-printed material, and (f) inkjet-printed antenna array on the top layer. *48*

Figure 3.8 (a) Measured and simulated output voltage with respect to different input power at 26 GHz for the embedded energy harvester and (b) Measured S_{11} for the antenna array. *50*

Figure 3.9 (a) Measured radiation pattern at 26 GHz for the antenna array and (b) The wireless performance measurement setup for the system. *51*

Figure 3.10 (a) The stack-up for the 5G broadband and miniaturized AiP design and (b) the fabrication process of the glass SAP. *52*

Figure 3.11 Prototypes of the proposed 5G broadband and miniaturized Yagi AiP (a) element and (b) array design. *54*

Figure 3.12 Measured and simulated (a) S_{11} and (b) gain of the 5G broadband and miniaturized Yagi AiP element. *55*

Figure 3.13 Measured and simulated normalized radiation patterns for Yagi AiP element at (a) 24.25 GHz E-plane, (b) 24.25 GHz H-plane, (c) 40 GHz E-plane, and (d) 40 GHz H-plane. *56*

Figure 3.14 Measured and simulated (a) S_{11} and (b) gain of the 5G broadband and miniaturized Yagi AiP array. *57*

Figure 3.15 Measured and simulated normalized radiation patterns for Yagi AiP array at (a) 24.25 GHz E-plane, (b) 24.25 GHz H-plane, (c) 40 GHz E-plane, and (d) 40 GHz H-plane. *58*

Figure 3.16 Diagram of the eggbox unit cell denoting the folding angles (a) and the printed cross-shaped conductive elements (b);

(c) Fabricated prototype of 6 × 6 cross-dipole eggbox FSS and corresponding incidence angles: normal incidence (blue), rotate *y*-axis (green), and rotate *x*-axis (red). *59*

Figure 3.17 Simulation and measurement results for (a) horizontal (*x*-axis) and (b) vertical (*y*-axis) polarization response for different folding angles. *61*

Figure 3.18 Simulation and measurement results for (a) horizontal (*x*-axis) and (b) vertical (*y*-axis) polarization response for different rotating angles. *62*

Figure 3.19 Fabrication process for Miura 3D/inkjet-printed structure. Comparison of SU-8 surface modification: (a) rough surface on curved area and (b) smooth surface with SU-8 buffer layer. *63*

Figure 3.20 (a) Perspective and top view of the multilayer Miura individual FSS element ("unit cell") design, (b, c) Fabricated prototype of the 8 × 10 multilayer Miura FSS. Simulated and measured frequency response for different folding angles, and (d) incident angles (e). *65*

Figure 3.21 (a) Diagram of the Rotman-based harmonic mmID. Characterization of gain and angular coverage for the Rotman lens operating at 14 GHz (b) and 28 GHz (c). Conversion loss of the doubler circuit (d). *67*

Figure 3.22 (a) Estimated angle-dependent harmonic RCS at 28 GHz and range of 5 m. (b) Measured received power of the fully passive harmonic mmID at EIRP = 48 dBm. *68*

Figure 3.23 (a) Schematic of the RF front end of the 60 GHz mmID with $W_p = 1.87$ mm, $L_p = 1.42$ mm, $d_s = 1.31$ mm, WTL = 0.59 mm, and $R_s = 1.62$ mm. (b) Flexible, inkjet-printed RF front end of mmID tag. *70*

Figure 3.24 (a) Measured S_{11} of 4 × 1 patch antenna array of mmID. (b) Phase difference of mmID load for bias of 0 and 0.8 V for phase-based modulation. *71*

Figure 3.25 (a) Schematic of the inkjet-printed resistive-based temperature sensor with total footprint of 2.89 cm x 1.0 cm. (b) $\%\Delta R$ vs. temperature of resistive based sensor. *72*

Figure 3.26 Estimated range and local temperature of the mmID as it passes the heat source. *73*

Figure 3.27 Scalability demonstration of the tile-based phased array. *74*

Figure 3.28 (a) Microstrip-to-microstrip transition and (b) Front view of the 4-tile array (c) Back view of the 4-tile array. *75*

Figure 3.29 Simulation and measurement results for a single tile phased array (a) and for the 2 × 2 tiles ("unit cell") phased array and (b). *76*

Figure 3.30 (a) Picture of the flexible Rotman lens-based antenna array and (b) measured (solid lines) and simulated (dashed lines) gains of the antenna array held in a planar position. *78*

Figure 3.31 (a) Picture of the fully flexible Rotman-based rectenna and (b) plot of the measured voltages and output powers versus incident power density for the Rotman-based rectenna. *79*

Figure 3.32 Simulated and measured voltages and output powers versus incident power density for the rectenna with and without the Rotman Lens. *80*

Figure 3.33 Measured harvested powers versus incidence angles for different curvatures. *81*

Figure 4.1 An example of mobile handsets and scenario of its attachment to the human head. *84*

Figure 4.2 Sub-6-GHz antenna which is small for the area of the platform (a) Geometry (b) S_{11} (c) Far field. *85*

Figure 4.3 Two sub-6-GHz antennas on the platform (a) Geometry (b) S-parameters (c) Far field. *86*

Figure 4.4 Four sub-6-GHz antennas on the platform (a) Geometry (b) S-parameters (c) Far field. *88*

Figure 4.5 Another sub-6-GHz antenna on the platform (a) Geometry (b) S_{11} (band-widened) (c) Far field. *89*

Figure 4.6 Two sub-6-GHz SRR antennas on the platform (a) Geometry (b) S-parameters (c) Far field. *90*

Figure 4.7 Four SRR antennas (a) Geometry (b) S-parameters (c) Far field (d) J_s (OGRRs) (e) J_s (SRRs). *91*

Figure 4.8 Sub-6-GHz wide-band antennas being tested for wireless links (a) Single wide-band type (b) Wide-band array type (c) Wide-band with channel selectivity (d) Wide-band without and with (e) channel selectivity. *93*

Figure 4.9 Antennas for links and channel selectivity (a) Test setup (b), (c) and (d) Channels f_1, f_2, and f_3 selected. *94*

Figure 4.10 Looking into the characteristics of sub-6-GHz antennas in the level of communication systems. *95*

Figure 4.11 Another type of wireless link test (a) Configuration (b) Entire system with the test elements. *97*

Figure 4.12 Antenna WB-α with the 5G UE (a) S_{11} (b) T.R antenna position and its screenshot of test result (c) other tested antenna positions. *98*

Figure 4.13 Antenna WB-β-T with the 5G UE (a) S_{11} (b) T.R antenna position and its screenshot of test result (c) other tested antenna positions. *100*

Figure 4.14 Ch.3 of antenna WB-β-F with the 5G UE (a) S_{11} (b) T.R antenna position and its screenshot of test result (c) other tested antenna positions. *102*

Figure 4.15 Ch.2 of antenna WB-β-F with the 5G UE (a) S_{11} (b) T.R antenna position and its screenshot of test result (c) other tested antenna positions. *103*

Figure 4.16 Ch.1 of antenna WB-β-F with the 5G UE (a) S_{11} (b) T.R antenna position and its screenshot of test result (c) other tested antenna positions. *105*

Figure 4.17 Imagination of crossover integrating 5G and satellite, and 5G and vehicular communication. *106*

Figure 4.18 A coaxial fed 1 × 4 array antenna (a) Back and front views (b) S_{11} (c) Far field in 3D. *107*

Figure 4.19 A situation where the phone has the 1 × 4 array antenna on top (a) Geometry in 3D (b) Far field. *108*

Figure 4.20 A line-fed 1 × 8 array antenna (a) Top-view (b) S_{11} (c) Far field in 3D. *109*

Figure 4.21 Progressive phasing for a 1 × 4 array antenna to tilt the beam (a) 1 × 2 array with a fixed beam (b) 1 × 4 array with a fixed beam (c) 1 × 4 array with beam tilting. *110*

Figure 4.22 mmWave microstrip beamforming antenna (a) Geometry (b) S_{ii} with $i = 1, 2, 3$ and 4 (c) Tilted beam. *111*

Figure 4.23 mmWave microstrip Rotman lens (a) Geometry (b) E-field for boresight (c) E-field for the tilted beam. *112*

Figure 4.24 Mimicking the waveguide (WG), SIWs are used for beamforming antennas (a) WG slot array antenna (b) Beam pattern of WG slot array antenna (c) SIW slot array example 1 (d) Beam pattern of SIW slot array example 1 (e) SIW slot array example 2 (f) Beam pattern of SIW slot array example 2. *113*

Figure 4.25 SIW beamforming antenna (a) Geometry vs. a smartphone (b) Modified geometry and on the palm (c) S_{ii} with $i = 1, 2, 3$ and 4

(d) E-field distribution with port 1 on (e) E-field distribution with port 2 on (f) Tilted beam (g) 3D view of the steered beam. *115*

Figure 4.26 SIW triple-band beamforming antenna (a) Unit slot array for one channel and the beam pattern (b) 27 GHz band (f_1) slot array selected by the f_1 filter with S_{11} and the beam pattern (b) 28 GHz band (f_2) slot array selected by the f_2 filter and the beam pattern (c) 29 GHz band (f_3) slot array selected by the f_3 filter and the beam pattern. *118*

Figure 4.27 Glass-based SIW beamforming antenna (a) Prototype (b) S_{ii} with $i = 1, 2, 3$ and 4 (c) Antenna is tested in the anechoic chamber (d) Steered beam pattern. *119*

Figure 4.28 Bigger array antennas for 5G infra (a) Series-fed microstrip array in the CAD program (b) Fabricated series-fed microstrip array (c) Highly populated array antenna as a candidate for the infra. *121*

Figure 4.29 Metamaterials to ease the shortcomings of conventional array antennas (a) From a curved lens to a metasurface lens (b) A design example of a flat lens and conversion in wave front (c) An ordinary slab becoming a metasurface beam bender (d) An example of a flat beam bender and the converted wave front. *123*

Figure 4.30 Metamaterial surface to increase the antenna gain (a) A single patch (b) Lower antenna gain of the single patch (c) Realized metasurface (d) Antenna gain improved by over 10 dB. *124*

Figure 4.31 Metamaterial surface to make the beam lean (a) Realized metasurface (b) Beam angle shifted to −30°. *125*

Figure 4.32 Metamaterial reflecting surface (a) Parabolic reflector vs. reflectarray (RA) (b) Single patch (c) Beam pattern of the single patch (d) Normal reflection RA (e) Far field pattern by the RA. *126*

Figure 4.33 Metamaterial reflecting surface for oblique reflection (a) Metasurface to tilt the reflected field (b) Effect of beam tilting by the reflecting metasurface. *129*

Figure 4.34 Two kinds of antenna measurement facilities (a) Anechoic chamber (b) Compact antenna test range (CATR). *130*

Figure 4.35 5G antenna under near field test (a) Entire view on the system (b) Elements from probe to AUT. *132*

Figure 4.36 NF test examples (a) NF of 1 patch (b) FF of the patch (c) NF of 30° titling by a 1×4 array (d) FF of 30° titling by the array (e) NF of 7.5° titling (f) FF of 7.5° titling (e) NF of −30° titling (f) FF of −30° titling. 133

Figure 4.37 NF test on a mmWave metasurface (a) Entire setup of the NF test with a beam bending metasurface (b) NF of 1 patch for 31 GHz (c) FF of the patch (d) NF of 20° titling by the metasurface (e) FF of 20° titling at 31 GHz. 135

Figure 4.38 CATR tests (a) Setup (b) (c) Patch FF vs. Metasurface FF (d) CATR FF vs. NF-to-FF in testing the patch (e) CATR FF vs. NF-to-FF in testing the beam bending metasurface. 137

Figure 4.39 Communication system level tests (a) Four possibilities of TX and RX beam directions (b) A horn and a patch on the line (H-P-A), Transmission coefficient (S_{21}) and 64-QAM constellation (c) A horn and a patch misaligned (H~P-Mis), S_{21} and 64-QAM constellation (d) A (−30°) rotated horn and a −30° beamformer aligned (−30°H~−30°BFP-A), S_{21} and 64-QAM constellation (e) A −15° rotated horn and a −15° beamformer aligned (−15°H~−15°BFP-A), S_{21} and 64-QAM constellation (f) A +15° rotated horn and a +15° beamformer aligned (+15°H~+15°BFP-A), S_{21} and 64-QAM constellation (g) A +30° rotated horn and a +30° beamformer aligned (+30°H~+30°BFP-A), S_{21} and 64-QAM constellation. 139

Figure 4.40 Examples of active RIS structures (a) Columns of switch loaded dipoles (b) Columns of a pair of loops (c) Rows of CPW resonators (d) A 2D array of crossed SIRs. 141

Figure 4.41 Examples of active RIS structures with new methods (a) Connected patches for route changing (b) LC-embedded multilayered device. 142

Figure 5.1 AUT H-plane radiation pattern measured in RC and in AC. 148

Figure 5.2 CATR measurement system setup, TX requirements. 149

Figure 5.3 CATR measurement system setup, RX requirements. 150

Figure 5.4 CATR measurement system setup, RX OTA dynamic range, ACS, general blocking, and narrowband blocking. 151

Figure 5.5 CATR measurement system setup, OTA RX intermodulation (IMD) 152

Figure 5.6 CATR measurement system setup for OTA in-channel selectivity (ICS). 153

Figure 5.7 CATR measurement system setup for time alignment error (TAE). 154

Figure 5.8 Probe/scanner near field systems: spherical, cylindrical, and planar. *155*
Figure 5.9 Far field range for an $N \times N$ array of $\lambda/2$ spaced elements. *155*
Figure 5.10 EMITE H-Series hybrid OTA Test System with CATR + DFF + SNF Test Methods. *156*
Figure 5.11 The antenna layout evolution on UEs. *157*
Figure 5.12 Hybrid thermal/electromagnetic test platform. *158*
Figure 5.13 Illustration of multiple physical transmission effects. *161*
Figure 5.14 Illustration of ASE with RR scheduler as a function of sectorization. *162*
Figure 5.15 Digital beamforming antenna patterns (a) and an illustration of BSNRI (b) *164*
Figure 5.16 An illustration of beamforming battery consumption (BBC). *165*
Figure 5.17 Example of a 5G device that overheats by intensive use of 5G. *166*
Figure 5.18 Example of a 5G device that uses a SW heat dissipation algorithm and switches to 4G when temperature reaches a predefined threshold. *166*
Figure 5.19 5G beamforming capacity gain measured using an EMITE F200 reverberation chamber. *168*
Figure 5.20 5G beamforming capacity gain measured using an EMITE H300 anechoic chamber. *169*
Figure 5.21 Cumulative distribution function (CDF) of the 5G beamforming capacity gain (BCG) measured using an EMITE H300 anechoic chamber. *170*
Figure 5.22 Beamforming averaged latency (BAL). *171*
Figure 5.23 5G gNB FR1 OTA E2EL measured using an EMITE F200 reverberation chamber. *171*
Figure 5.24 5G gNB FR1 OTA RF latency measured using an EMITE F200 reverberation chamber. *172*
Figure 5.25 5G gNB FR1 OTA average TCP throughput measured with an EMITE F200 reverberation chamber. *173*
Figure 5.26 5G FR1 TTPUT. *175*
Figure 5.27 5G FR1 PDLT. *175*
Figure 5.28 5G FR1 PULT. *176*

Figure 6.1 AiP simulated pattern (a) radiation pattern for five beam-steering angles *ø*. (b) beam-steering pattern defined. *183*

Figure 6.2 Experimental setup in the measurement campaign. (a) photograph in an anechoic chamber (b) illustration of beam-steering. *184*

Figure 6.3 Element discrepancies of AiP obtained in the two modes. *186*

Figure 6.4 Beam-steering patterns of an AiP on two planes after the two calibration modes. (a) *xy* plane (b) *xz* plane. *187*

Figure 6.5 Experimental setup in the measurement campaign. (a) photograph in an anechoic chamber (b) illustration of measurement setup. *190*

Figure 6.6 Array calibration results using the improved (proposed) and original (reference) methods. *191*

Figure 6.7 Experimental setup photograph inside a compact range chamber for calibration validation. *192*

Figure 6.8 RMSD with the proposed method in a three-probe setup via locating side probes in different directions for various Ψ. *193*

Figure 6.9 Diagram of MPAC for FR1. *197*

Figure 6.10 Diagram of RTS for FR1. *198*

Figure 6.11 Diagram of 3D MPAC for FR2. *201*

Figure 6.12 The four standard NR channel models, namely (a) FR1 UMi CDL-A, (b) FR1 UMa CDL-C, (c) FR2 InO CDL-A, and (d) FR2 UMi CDL-C. It should be noted that the two FR1 channel models lack elevation modeling for the incoming paths, meaning that all clusters arrive at an elevation of 0° with no variation in elevation spread, and are therefore 2D. *206*

Figure 6.13 Spatial correlation channel model validation options. *207*

Figure 6.14 Target and emulated spatial correlation in test zone. *208*

Figure 6.15 Target and emulated PAS seen by the DUT in test zone. *209*

Figure 6.16 Practical MPAC measurement chambers (a) FR1, (b) FR2. *211*

Figure 6.17 DL TPUT vs. azimuth degrees in −80 dBm and −105 dBm for FR1. *212*

Figure 6.18 UL TPUT vs. azimuth degrees in −95 dBm and −105 dBm for FR1. *213*

Figure 6.19 Average DL TPUT at different test points vs. RSRP for FR2. *214*

Figure 6.20 Average DL TPUT at different test points vs. SNR set by CE for FR2. *215*

Figure 6.21 H300 IFF-CATR test system by EMITE. *216*

Figure 6.22 LTE link antenna for an IFF-CATR test system. *217*

Figure 6.23 Working principle of the IFF-CATR test method. *218*

Figure 6.24 Serrated-edges reflector (a) vs. rolled-edges reflector (b). *219*

Figure 6.25 CATR power transfer function. *220*

Figure 6.26 Phase curvature within the CATR QZ. *221*

Figure 6.27 CATR when DUT is in transmit mode. *222*

Figure 6.28 CATR-QZ ripple test (field distribution) set up (courtesy of EMITE). *224*

Figure 6.29 Vertical-cut CATR amplitude reciprocity (courtesy of EMITE). *225*

Figure 6.30 Vertical-cut CATR phase reciprocity (courtesy of EMITE). *225*

Figure 6.31 Fine beam peak direction search grid. (a) identify the measurement grid points that yielded EIRP values within the fine search region. (b) placement of fine beam peak direction search grid points. *225*

Figure 6.32 Some final ripple test results for a commercial CATR test system (courtesy of EMITE). *227*

Figure 6.33 Rx beam peak search for an NR NSA Band 66 + Band 260 UE measured with a commercial CATR (courtesy of EMITE). *229*

Figure 6.34 Tx beam peak search for an NR NSA Band 66 + Band 260 UE measured with a commercial CATR (courtesy of EMITE). *230*

Figure 6.35 TRP for an NR UE measured with a commercial CATR (courtesy of EMITE). *230*

Figure 6.36 3D EIRP for an NR FR1 + FR2 UE measured with a commercial CATR (courtesy of EMITE). *231*

Figure 6.37 DFF and IFF-CATR for simultaneous FR1+FR2 NR OTA testing at the H-Series Test System by EMITE (courtesy of EMITE). *231*

Figure 6.38 Throughput and thermal response of an NR FR2 UE measured in a commercial CATR with thermal module (courtesy of EMITE). *232*

About the Authors

Main Authors

David A. Sánchez-Hernández, PhD, is a full Professor holding the Antennas & Propagation and 5G Chair position at Universidad Politécnica de Cartagena, Spain, and founder of EMITE Ingeniería, S.L., Spain.

Steven R. Best, PhD, is Senior Principal Electromagnetics and Sensor Systems Engineer with The MITRE Corporation, located in Bedford, MA, USA.

Manos M. Tentzeris, PhD, is a Ed and Pat Joy Chair Professor on Antennas in the area of flexible electronics with the School of ECE, Georgia Tech., USA.

Sungtek Kahng, PhD, is Professor with Incheon National University, Head of Korea's Ministry of Science and ICT-sponsored research and development center on RF and Satellite Communication, and Executive Director at the Korean Institute of Communication and Information Science and the Korean Institute of Electrical Engineering, South Korea.

Gert F. Pedersen, PhD, is currently a Full Professor heading the Antenna, Propagation and Millimeter-Wave Systems Networking Laboratory at Aalborg University, Denmark.

Contributing Authors

Charles Lynch is currently pursuing the MS and PhD degrees in electrical engineering with the Georgia Institute of Technology, Atlanta, GA, USA, and a Research Assistant with the ATHENA Group, Georgia Institute of Technology. At the 2023 IEEE IMS conference, he received the audience choice in the 3MT Competition.

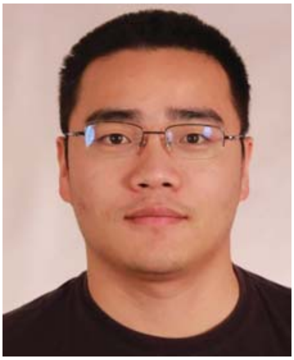

Wei Fan, PhD, is currently a full Professor with the National Mobile Communications Research Laboratory, School of Information Science and Engineering, Southeast University, Nanjing, China.

Foreword

In the ever-evolving landscape of communication technology, antennas have undergone a profound transformation, surpassing their traditional roles confined to line-of-sight scenarios and transcending their traditional roles in line-of-sight scenarios. The advent of 5G, with its unprecedented demands for high data throughput and low latency, has obliterated the once-distinct boundary between RF antennas and signal processing subsystems. Antennas now stand as integral components within communication systems, permeating various scenarios, from wireless systems leveraging multipath propagation to the connectivity fabric of Internet of Things (IoT) devices. This shift highlights the critical role antennas play in laying the groundwork for seamless communication.

This book elucidates the advancements essential to meet the challenges posed by 5G and serves as a pioneering roadmap for the future of communication systems, specifically laying the groundwork for the anticipated 6G era. The authors, distinguished experts in the field of antenna technology, have meticulously crafted a comprehensive exploration that extends beyond the current 5G landscape. Through insightful analysis, innovative design methodologies, cutting-edge testing techniques, and advancements in fabrication processes, this book not only addresses the challenges posed by current communication standards but also anticipates the demands of the forthcoming 6G paradigm.

Through the in-depth analysis provided within these pages and by seamlessly integrating theoretical insights with practical applications, the authors offer a holistic view of the analytical framework required for the design and implementation of antennas in the context of future communication technologies.

Moreover, the book delves into advanced design principles, showcasing novel approaches and methodologies that transcend the limitations of current systems. It introduces readers to cutting-edge testing methods specifically tailored for the unique demands of 5G radios and antennas, ensuring a robust evaluation framework for the next generation of communication technologies.

In the realm of fabrication, the book explores emerging techniques and materials, offering a glimpse into the future of antenna technology. By addressing fabrication challenges and presenting innovative solutions, the authors contribute to the foundational knowledge essential for the realization of sophisticated 6G communication systems.

The authors of this book stand as formidable authorities in the field of antenna technology. With distinguished academic backgrounds, extensive research contributions, and a wealth of professional experience, they managed to position this book as a comprehensive and authoritative resource in the field of 5G antenna technology and communications.

As a result, this book stands not only as a current reference for 5G antenna technologies but also as a visionary guide, paving the way for the forthcoming 6G communication systems. It is a testament to the authors' forward-thinking approach, providing readers with the analytical tools, design principles, testing methodologies, and fabrication insights necessary to shape the trajectory of communication systems in the years to come.

November, 2023

Christos Christodoulou
Director, COSMIAC@UNM
IEEE Life Fellow
Distinguished Professor
The University of New Mexico

Acknowledgements

The reason why this book was completed was the persistence, support, and help of many people who we would like to gratefully acknowledge here. Thank you to **Aileen Storry**, **Victoria Bradshaw**, **Margaret Cummins,** and **Indirakumari Sandilyan** at Wiley, your very nice patience and your valuable comments have triggered our motivation throughout the process, you are very professional and it has been a real pleasure to work with you on the publication of this book.

The authors are also particularly grateful to those who have also contributed to some extent by providing graphs, pictures, and also very good technical comments, in particular to **José Antonio Ypiña**, **Miguel Á. García-Fernández**, **Huaqiang Gao**, **Tong-Hong Lin**, **Marvin Joshi**, **Kexin Hu**, **Genaro Soto-Valle Angulo**, **I-Ting Chen**, **Yejune Seo**, **Changhyeong Lee,** and **Heejun Park**, your support and help has been a key for finalizing this book. Also, all the research work could not be possible without public and private funding. The authors would like to acknowledge the funding from Korea's state-run research institutes such as ETRI, KARI, KIMM, CAMM, KETI, and ADD and prestigious electronics and IT companies like NISSHA and Corning from Japan and USA, respectively, for R&D projects for film-based and Glass-based 5G antennas, EMITE Ingeniería, S.L. for providing full support and test systems used in this work, the Spanish Regional Development Fund (ERDF), NSF, and NextFlex for providing the funds that any top high-tech research needs.

The authors would like to honor **Samuel L. Katz**, a developer of the measles vaccine, **Beryl Benacerraf**, pioneer in the use of prenatal ultrasound, **Audrey Evans**, cancer specialist who gave many a home, **Nick Holonyak**, pioneer of LED lighting, **Maarten Schmidt**, first astronomer to identify a quasar, **Raymond Damadian**, creator of the first M.R.I. scanner, **Kamoya Kimeu**, whose discovered bones rewrote how we understand human evolution, **James Lovelock**, whose theory saw the earth as alive, **Robert F. Curl Jr**., a Nobel Prize winner who discovered unexpectedly simple carbon molecules called buckyball, and spurred explorations of nanotech, **Vladimir Zelenko**, who promoted

an unfounded Covid treatment, **Ken Knowlton**, who laid the groundwork for today's computer-generated imagery in film and on TV, **Sophie Freud**, Sigmund Freud's last surviving grandchild, who argued that psychoanalysis was a "narcissistic indulgence," **Ben Roy Mottelson**, Nobel Prize winner who discovered forces that can distort the shape of an atomic nucleus, **Ursula Bellugi**, pioneer in the world of sign language**, Sidney Altman**, Nobel Prize winner for finding that RNA was not just a carrier of genetic information but also a trigger life-changing chemical reactions in cells, **Arthur D. Riggs**, the inventor of artificial insulin, **Martin Pope**, whose research lit up electronic screens, **Stephen Wilhite**, creator of the GIF, **Donald Pinkel**, developer of a cure for childhood leukemia, **David Boggs**, coinventor of Ethernet, **Paul Farmer**, who grew a vast network of clinics serving some of the world's poorest communities, **Herbert Benson**, a cardiologist who saw that a person can influence bodily health through meditation, **Luc Montagnier**, Nobel Prize winner for co-discovering H.I.V., **Beatrice Mintz**, who found that nearby tissue could help tame tumor cells more gently than radiation or chemotherapy and paved the way to new therapies, **Richard Leakey**, whose discoveries helped cement Africa's standing as the cradle of humanity, **Mauro Forghieri**, whose transverse gearbox, flat-12 engine and sharky designs creations lead Scuderia Ferrari to four drivers' championships, seven constructors' titles, and 54 GP victories, **Martin Pope**, whose research on organic insulators and semiconductors led to the conversion of electricity into light and vice versa, **Ralph G Pearson**, who development the concept of hard and soft acids and bases (HSAB), and to **John Goodenough**, the Nobel Prize winner who helped transform lithium-ion batteries, **Max Fordham**, pioneer of sustainable building design, **William E. Stoney Jr.**, lead engineer on the Apollo NASA program, **David A. Hodges**, an absolute reference in any institution respect to education and research in integrated circuit (IC) design, **Henry Petroski**, who demystified engineering with literary examinations of the designs and failures of large structures as well as everyday items like the pencil and the toothpick, **James Lovelock**, creator of the Gaia theory, which laid the foundations for Earth system science and a new understanding of the interplay between life, clouds, rocks, and the atmosphere, **Evelyn M. Witkin**, whose SOS response in DNA mutagenesis has led to current DNA repair, **Joan H. van der Waals**, whose partition function determined that neighboring guest gas molecules cannot interact, and all the other scientists who died in 2022 and what has gone out of 2023 at the time of writing this book, because none of them made Wikipedia's list of celebrities, yet their passion for science has made this world certainly a much better place for everybody else.

Finally, the authors are also in an invaluable debt with **Marien**, **Maria-Eleni**, **Shujin**, **Nahmjoo**, and **Mary**, our beloved partners, and to **Lucía**, **Mario**,

Bruno, **Markella-Rena**, **Christina-Apostolia**, **Henry**, **James**, **Uhdahm**, **Minsaw**, **Seokhwan**, **Jongsoon**, **Taeja**, **Hakyong**, **Matthew, Daniel, Katherine and Gregory**, our descendants, as time was taken from them to allow us for writing this book without any complaint, something we keep admiring in disbelief throughout the years.